## Open channels and radiation trapping eigenstates in complex resonant media

Romain Rescanieres , Romain Pierrat, and Arthur Goetschy ESPCI Paris, PSL University, CNRS, Institut Langevin, 1 rue Jussieu, F-75005 Paris, France

(Received 9 December 2024; accepted 25 July 2025; published 23 September 2025)

We present a statistical study of the transmission and dwell-time matrices in disordered media composed of resonators, focusing on how frequency detuning influences their eigenvalue distributions. Our analysis reveals that the distribution of transmission eigenvalues undergoes a transition from a monomodal to a bimodal profile, and back to monomodal, as the frequency approaches the resonant frequency of the particles. Moreover, the distribution of dwell-time eigenvalues broadens significantly near resonance, with the longest lifetimes exceeding the median by several orders of magnitude. These results are explained by examining how frequency  $\omega$  affects the transport mean free path of light  $\ell(\omega)$  and the energy transport velocity  $v_E(\omega)$ , which in turn shape the observed distributions. We demonstrate the strong potential of wavefront shaping to synthesize wavefronts associated with eigenstates that enhance transmission and energy storage (or radiation trapping) in resonant disordered media. In the diffusive regime, where the system thickness L exceeds the mean free path, both transmission and dwell time can be enhanced by a factor  $\propto L/\ell(\omega) \gg 1$  when using wavefronts associated with the largest eigenvalues instead of plane waves. In the localized regime, the enhancements become  $\propto Ne^{2L/\xi}$  for transmission and  $\propto N\xi/L$  for dwell time, where  $\xi$  is the localization length and N is the number of controlled scattering channels. Finally, we show that employing high-Q resonators instead of low-Q ones increases energy storage within the medium by a factor of  $\propto Q/k\ell(\omega)$  in both the diffusive and localized regimes.

DOI: 10.1103/wqrf-tkty

#### I. INTRODUCTION

In recent years, the development of wavefront shaping techniques has enabled the measurement of the scattering matrix in various complex media, such as disordered waveguides [1-3], scattering slabs [4,5], multimode fibers [6-8], and biological tissues [9,10], which can support a large number of propagation channels. These advancements have shown that specific wavefronts can be focused deep within turbid systems or fully transmitted through materials that are otherwise opaque to plane waves [11,12]. Additionally, by calculating the derivative of the scattering matrix with respect to frequency, it is possible to construct the Wigner-Smith operator and the associated dwell-time operator, whose eigenvalues represent the duration a quasimonochromatic wave packet can spend within an open system [13,14]. Using a spatial light modulator to generate the eigenstates of the dwell-time operator, it is thus in principle possible to optimize the energy stored in any arbitrary complex system [15].

So far, these properties have been established in nonresonant scattering materials. However, resonant media are now ubiquitous in nanophotonics and atomic optics. Technological advancements have enabled the creation of optically resonant

Published by the American Physical Society under the terms of the Creative Commons Attribution 4.0 International license. Further distribution of this work must maintain attribution to the author(s) and the published article's title, journal citation, and DOI.

systems structured either at the wavelength scale (such as photonic crystals and arrays of microcavities) or at a deep subwavelength scale (such as plasmonic nanoresonators and atomic arrays). Light-matter interactions in these systems are typically described in terms of collective modes rather than by their scattering matrices [16–22]. Furthermore, the effect of coherent control via wavefront modulation on such media has been scarcely explored. Previous research has examined a few resonant elements embedded in otherwise nonresonant materials, such as using resonators to focus light deep into complex media without a guide star [15,23] or employing fluorescent probes to resolve the three-dimensional (3D) profile of open channels in a nonresonant disordered slab [24]. In contrast, this work addresses systems where all scattering units are resonant, aiming to understand the influence of local resonances on the properties of transmission and dwell-time matrices.

The impact of resonant scattering on simple plane wave propagation is relatively well understood, as demonstrated in a variety of disordered systems, ranging from cold atomic gases [25] to random dielectric materials supporting Mie resonances [26], as well as acoustical systems made of droplets [27] or Helmholtz resonators [28]. Internal resonances are known to affect both stationary and dynamic transport properties. The ability to tune the refractive index near resonance allows for significant variations in the phase and group velocities that characterize the propagation of the ballistic wave [27,29]. However, in a disordered scattering medium, most of the energy is carried by the diffusive component rather than the ballistic wave component. This diffusive component propagates at a speed  $v_E \leqslant c$  for all frequencies and can be

<sup>\*</sup>Contact author: arthur.goetschy@espci.psl.eu

dramatically slowed down near resonance [30], giving rise to spectacular radiation trapping in atomic gases [25,31–33]. Additionally, the scattering cross section of the resonators increases significantly near resonance, reducing the transport mean free path  $\ell$  and mean transmission coefficient  $\langle T \rangle$ , while substantially increasing the time needed to cross the sample, termed the Thouless time  $\tau_{\rm Th}$ . The objective of this work is to extend the analysis beyond plane wave behavior to arbitrary wavefronts, whose propagation cannot be adequately explained by the traditional diffusion model, even when the sample thickness L greatly exceeds  $\ell$  [34].

To address this problem, we consider light wave propagation in an assembly of pointlike resonators randomly distributed within a finite volume much larger than the wavelength. For convenience, this volume is placed in a waveguide, which limits the size of the studied matrices to the number of propagating modes in the waveguide. Section II focuses on establishing the coupled equations describing light-matter interactions and the procedure for constructing the transmission and reflection matrices from these equations. It also presents the results of numerical simulations of the transmission matrix, evaluated at different frequencies and across numerous disorder configurations. The statistical properties of transmission eigenvalues and eigenstates as a function of frequency  $\omega$  are shown to depend crucially on the mean free path  $\ell(\omega)$ , allowing for the exploration of different propagation regimes (quasiballistic, diffusive, localized). In a symmetric fashion, Sec. III presents results related to the dwell-time operator, demonstrating that the behavior of eigenvalue distribution and eigenstate propagation can be understood through the interplay between the frequency-dependent mean free path  $\ell(\omega)$  and energy velocity  $v_E(\omega)$ . Section IV provides a summary of the results, emphasizing the significant advantages of wavefront shaping in achieving much higher transmission and energy storage compared to simple plane wave propagation, in both the diffusive and localized regimes.

### II. TRANSMISSION MATRIX AND OPEN CHANNELS

# A. Transmission and reflection matrices for resonant scattering media

The system under study consists in an assembly of  $N_s$  identical pointlike resonant scatterers of polarizability  $\alpha(\omega)$ , randomly distributed in a two-dimensional (2D) waveguide of thickness L and width W, as sketched in Fig. 1. It is illuminated from the left by waves of frequency  $\omega=ck$ , polarized along the z direction. This two-dimensional configuration can be interpreted as a system and sources invariant along the z direction. While this choice is primarily motivated by numerical convenience, the main results of this study are expected to remain valid in more general, three-dimensional scenarios. Possible experimental implementations of the system are discussed in the concluding remarks.

In order to compute the transmission matrix and dwell-time operator, we need to evaluate the scalar Green's function of the wave equation,  $G(\mathbf{r}, \mathbf{r}', \omega)$ , for a source located at any point  $\mathbf{r}' = (x', y')$  on the front surface of the medium and an observation point  $\mathbf{r} = (x, y)$  located either on the back surface or on the front surface. In Appendix A, we demonstrate that,

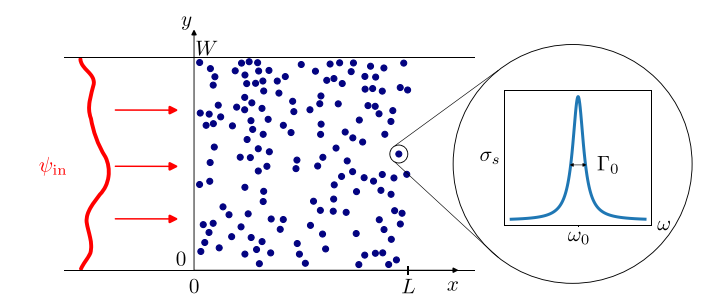


FIG. 1. Schematic representation of the system under study.  $N_s$  resonant scatterers are uniformly distributed in a region of size  $L \times W$  of a 2D waveguide. An incident field  $\psi_{\rm in}$  at frequency  $\omega$  is sent onto the scattering region from the left. The resonant scatterers, here represented with a finite size, will be taken to be pointlike in the rest of this paper. Their quality factor is  $Q = \omega_0/(\Gamma_0/2)$ . The inset shows the scattering cross section  $\sigma_s = k^3 |\alpha(\omega)|^2/4$  of a single resonator in free space, with polarizabilty  $\alpha(\omega)$  given by Eq. (5).

in the presence of the waveguide, the coupled dipole equations governing the evolution of  $G(\mathbf{r}, \mathbf{r}', \omega)$  can be expressed in the following form:

$$G(\mathbf{r}, \mathbf{r}', \omega) = \tilde{G}_0(\mathbf{r}, \mathbf{r}', \omega) - k^2 \sum_{i=1}^{N_s} \tilde{G}_0(\mathbf{r}, \mathbf{r}_i, \omega) \tilde{\alpha}(\mathbf{r}_i, \omega) \tilde{\psi}_i,$$
(1)

$$\tilde{\psi}_i = \tilde{G}_0(\mathbf{r}_i, \mathbf{r}', \omega) - k^2 \sum_{\substack{j=1\\j\neq i}}^{N_s} \tilde{G}_0(\mathbf{r}_i, \mathbf{r}_j, \omega) \tilde{\alpha}(\mathbf{r}_j, \omega) \tilde{\psi}_j. \quad (2)$$

Here,  $\tilde{\psi}_i$  is the z-component of the field exciting the scattering dipole at the position  $\mathbf{r}_i$ . Note that no electric dipoles appear explicitly in these equations, as they were replaced by their expressions  $p_i = \varepsilon_0 \tilde{\alpha}(\mathbf{r}_i, \omega) \tilde{\psi}_i$  to simplify the formulation. Nevertheless, we refer to Eqs. (1) and (2) as the coupled dipole equations henceforth. Furthermore,  $\tilde{G}_0(\mathbf{r}, \mathbf{r}', \omega)$  is the retarded Green's function of the wave equation in the empty waveguide, which solves  $(\nabla^2 + k^2 + i0^+)\tilde{G}_0(\mathbf{r}, \mathbf{r}', \omega) = \delta(\mathbf{r} - \mathbf{r}')$ . The presence of the waveguide imposes Dirichlet boundary conditions in the y direction, yielding

$$\tilde{G}_0(\mathbf{r}, \mathbf{r}', \omega) = \frac{1}{W} \sum_{m \geq 0} \sin\left(\frac{n\pi y}{W}\right) \sin\left(\frac{n\pi y'}{W}\right) \frac{e^{ik_n|x - x'|}}{ik_n}, \quad (3)$$

where  $k_n = k\sqrt{1 - (n\pi/kW)^2}$ . Note also that the expression of the polarizability  $\tilde{\alpha}(\mathbf{r}_i, \omega)$  of each scatterer i is modified compared to its free space value  $\alpha(\omega)$ . It is given by (see Appendix A)

$$\frac{1}{\tilde{\alpha}(\mathbf{r}_i, \omega)} = \frac{1}{\alpha(\omega)} + k^2 \Delta G_0(\mathbf{r}_i, \omega), \tag{4}$$

where  $\Delta G_0(\mathbf{r}_i, \omega) = \tilde{G}_0(\mathbf{r}_i, \mathbf{r}_i, \omega) - G_0(\mathbf{r}_i, \mathbf{r}_i, \omega)$ , with  $G_0$  the retarded free space Green's function. For z-polarized waves in 2D, the bare polarizability reads

$$\alpha(\omega) = \frac{-4c^2 \Gamma_0/\omega_0}{\omega^2 - \omega_0^2 + i\Gamma_0 \omega^2/\omega_0},\tag{5}$$

where  $\omega_0$  and  $\Gamma_0$  are, respectively, the resonant frequency and line width in free space (see inset of Fig. 1). This expression satisfies the condition  $\text{Im}[1/\alpha(\omega)] = k^2 \text{Im}[G_0(\mathbf{r}_i, \mathbf{r}_i, \omega)]$ , imposed by energy conservation of the scattering free space. In addition,  $G_0(\mathbf{r}, \mathbf{r}', \omega) = -(i/4)H_0^{(1)}(k|\mathbf{r} - \mathbf{r}'|)$ , with  $H_0^{(1)}$  the Hankel's function of the first kind of order 0. The numerical procedure used to evaluate  $\Delta G_0(\mathbf{r}_i, \omega)$  efficiently is detailed in Appendix B.

Consequently, replacing free space with a waveguide means not only replacing the free space retarded Green's function  $G_0$  with  $\tilde{G}_0$  in the coupled dipole equations, but also renormalizing the polarizability. This renormalization is essential to satisfy the energy conservation condition  $\text{Im}[1/\tilde{\alpha}(\mathbf{r}_i,\omega)]=k^2\text{Im}[\tilde{G}_0(\mathbf{r}_i,\mathbf{r}_i,\omega)]$  in the waveguide. The local polarizability can also be expressed as

$$\tilde{\alpha}(\mathbf{r}_i, \omega) = \frac{-4c^2 \Gamma_0/\omega_0}{\omega^2 - \tilde{\omega}_0(\mathbf{r}_i)^2 + i\tilde{\Gamma}_0(\mathbf{r}_i)\omega^2/\omega_0},$$
 (6)

where  $\tilde{\omega}_0(\mathbf{r}_i)^2 = \omega_0^2 + 4\omega^2 \Gamma_0 \text{Re}[\Delta G_0(\mathbf{r}_i,\omega)]/\omega_0$  and  $\tilde{\Gamma}_0(\mathbf{r}_i) = -4\Gamma_0 \text{Im}[\tilde{G}_0(\mathbf{r}_i,\omega)]$ . In the waveguide, translation invariance is broken, so that both the Lamb shift and decay rate, proportional to the local density of state, depend on the position  $\mathbf{r}_i$  of the resonator.

We can express now the transmission matrix  $\mathbf{t}(\omega)$  and reflection matrix  $\mathbf{r}(\omega)$  of the disordered medium using a basis composed of the  $N = \lfloor kW/\pi \rfloor$  propagating channels of the empty waveguide. These channels are represented by the functions  $e^{ik_nx}\xi_n(y)$ , with  $\xi_n(y) = \sqrt{2/W}\sin(n\pi y/W)$ . After normalizing each state by its flux,  $\varepsilon_0 ck_n/2k$ , the elements of the  $N \times N$  transmission and reflection matrices can then be determined through the Fisher-Lee relations [35],

$$t_{mn}(\omega) = 2i\sqrt{k_m k_n} \langle L, \xi_m | \mathbf{G}(\omega) | 0, \xi_n \rangle, \tag{7}$$

$$r_{mn}(\omega) = -\delta_{mn} + 2i\sqrt{k_m k_n} \langle 0, \xi_m | \mathbf{G}(\omega) | 0, \xi_n \rangle, \tag{8}$$

where the Green's operator  $\mathbf{G}(\omega)$  is defined through its realspace representation,  $\langle \mathbf{r} | \mathbf{G}(\omega) | \mathbf{r}' \rangle = G(\mathbf{r}, \mathbf{r}', \omega)$ . The choice of normalization guarantees that the matrices  $\mathbf{t}(\omega)$  and  $\mathbf{r}(\omega)$ satisfy the condition

$$\mathbf{t}(\omega)^{\dagger}\mathbf{t}(\omega) + \mathbf{r}(\omega)^{\dagger}\mathbf{r}(\omega) = \mathbf{1} \tag{9}$$

in the absence of absorption. This flux conservation condition is only satisfied if the dressed polarizabilty  $\tilde{\alpha}(\mathbf{r}_i, \omega)$  is used in the evaluation of the Green's operator; it is not satisfied if the bare polarizability  $\alpha(\omega)$  is used instead.

In order to compute the transmission and reflection matrices through Eqs. (7) and (8), the evaluation of the Green's operator is needed. According to Eqs. (1) and (2), we can write it in the form

$$\mathbf{G}(\omega) = \tilde{\mathbf{G}}_{\mathbf{0}}(\omega) + \tilde{\mathbf{G}}_{\mathbf{0}}(\omega) \mathbb{T}(\omega) \tilde{\mathbf{G}}_{\mathbf{0}}(\omega), \tag{10}$$

where the collective  $\mathbb{T}$  operator is defined as

$$\mathbb{T}(\omega) = -k^2 \sum_{i=1}^{N_s} \sum_{j=1}^{N_s} \left[ \mathbb{A}(\omega) \frac{\mathbb{1}}{\mathbb{1} + k^2 \mathbb{G}_0(\omega) \mathbb{A}(\omega)} \right]_{ij} |\mathbf{r}_i\rangle \langle \mathbf{r}_j|.$$

Here,  $\mathbb{A}(\omega)$  and  $\mathbb{G}_0(\omega)$  are  $N_s \times N_s$  matrices, defined as  $\mathbb{A}_{ij}(\omega) = \tilde{\alpha}(\mathbf{r}_i, \omega)\delta_{ij}$  and  $\mathbb{G}_{0,ij}(\omega) = (1 - \delta_{ij})\tilde{G}_0(\mathbf{r}_i, \mathbf{r}_j, \omega)$ .

Fisher-Lee relations (7) and (8) along with Eq. (10) reveal that the matrices  $\mathbf{t}(\omega)$  and  $\mathbf{r}(\omega)$  can be computed directly in the constant-flux basis from the combination of the matrices  $A(\omega)$  and  $G_0(\omega)$  with the propagators  $\langle x, \xi_m | \tilde{\mathbf{G}}_{\mathbf{0}}(\omega) | 0, \xi_n \rangle = \delta_{mn} e^{ik_m x} / 2ik_m$  and  $\langle x, \xi_m | \tilde{\mathbf{G}}_{\mathbf{0}}(\omega) | \mathbf{r}_i \rangle = \xi_m (y_i) e^{ik_m |x-x_i|} / 2ik_m$ . Explicitly, Eqs. (7) and (8) can be rewritten as  $t_{mn}(\omega) = 2i\sqrt{k_m k_n} G_{mn}(L,\omega)$  and  $r_{mn}(\omega) = -\delta_{mn} + 2i\sqrt{k_m k_n} G_{mn}(0,\omega)$ , where  $G(x,\omega)$  is a  $N \times N$  matrix that reads

$$\mathbb{G}(x,\omega) = \mathbb{B}(x,\omega)$$
$$-k^2 \mathbb{C}(x,\omega) \mathbb{A}(\omega) \frac{1}{1 + k^2 \mathbb{G}_0(\omega) \mathbb{A}(\omega)} \mathbb{C}^T(x,\omega),$$
(12)

with  $\mathbb{B}_{mn}(x,\omega) = \delta_{mn}e^{ik_mx}/2ik_m$  and  $\mathbb{C}_{mi}(x,\omega) = \xi_m(y_i)e^{ik_m|x-x_i|}/2ik_m$ .  $\mathbb{B}(x,\omega)$  is a  $N\times N$  square matrix, whereas  $\mathbb{C}(x,\omega)$  is an  $N\times N_s$  rectangular matrix. The simulation results presented in the following sections were obtained using this procedure, whose simulation cost depends only on  $N_s$  and N. It is in particular completely independent of the system length L. Indeed, the advantage of the coupled dipole method is that it does not require discretization of space, as is the case with other methods such as the recursive Green's function method.

#### B. Transmission eigenvalue distribution

Our goal is to study the impact of the detuning  $\delta = 2(\omega - \omega_0)/\Gamma_0$  on the distribution of the eigenvalues  $T_n$  of the matrix  $\mathbf{t}(\omega)^{\dagger}\mathbf{t}(\omega)$ . This distribution is defined as

$$P(T) = \frac{1}{N} \left\langle \sum_{n=1}^{N} \delta(T - T_n) \right\rangle. \tag{13}$$

In order to explore different propagation regimes by simply tuning the frequency, we focus our analysis to systems of width  $W \lesssim N\ell(\omega)$ , for which the localization length is  $\xi \simeq \pi N\ell(\omega)/2$  [36]. Since  $N \simeq kW/\pi$ , this imposes that  $k\ell(\omega) \gtrsim 1$ . In this regime, an estimate of the mean free path is  $\ell(\omega) = 1/\rho \sigma_s(\omega)$ , with  $\rho = N_s/LW$  the density of scatterers and  $\sigma_s(\omega)$  their scattering cross section; see Fig. 1 for an illustration. Explicitly, this gives [37,38]

$$k\ell(\omega) = \frac{4}{\rho k^2 |\alpha(\omega)|^2} \underset{\delta \ll Q}{\sim} \frac{(kW)(kL)}{4N_s} (\delta^2 + 1). \tag{14}$$

Reaching the diffusive regime  $\xi\gg L\gg\ell(\omega)$  requires a large number N of propagating channels, while reaching the localized phase close to resonance  $(W\lesssim N\ell(\omega_0)\lesssim L)$  requires a number of scatterers  $N_s$  such that  $(kW)(kL)\gtrsim N_s\gtrsim (kW)^2$ . All those requirements will be met in the following results. Figure 2 shows the distribution P(T) at different detunings  $\delta$ , in a waveguide supporting  $N\simeq 50$  channels  $(k_0W=161)$  filled with  $N_s=2\times 10^4$  scatterers of quality factor  $Q=\omega_0/(\Gamma_0/2)=10^3$ . Each value of detuning corresponds to a different transport regime, as reported in Table I.

For large detuning ( $\delta = 50$ ), the coupling between light and matter is weak. As a result, the mean free path, given by Eq. (14), exceeds the medium's thickness, causing most waves to undergo quasiballistic transport. Consequently, the transmission eigenvalue distribution P(T), shown in Fig. 2 (shaded

TABLE I. Correspondence between detuning value  $\delta$ , mean free path  $\ell$ , and localization length  $\xi$ , normalized by the system thickness L. The values are given for the parameters used in the numerical simulations shown in Figs. 2 and 4, namely,  $k_0L = 5000$ ,  $k_0W = 161$ , and  $N_s = 2 \times 10^4$ . For each detuning, the values of  $\ell/L$  and  $\xi/L$  determine the transport regime in the system.

Transport regime	Localized	Quasilocalized	Diffusive	Quasiballistic
$\frac{\delta}{\frac{\ell}{L}} \propto \frac{N}{N_s} (\delta^2 + 1)$	$0.5$ $2.5 \times 10^{-3}$	$\frac{2}{1.0 \times 10^{-2}}$	$8 \\ 1.3 \times 10^{-1}$	50 5.0
$\frac{\xi}{L} \propto \frac{N^2}{N_s} (\delta^2 + 1)$	$2.0\times10^{-1}$	$8.0 \times 10^{-1}$	$1.0 \times 10^{1}$	$4.2 \times 10^{2}$

green), is peaked around 1, with a minimum eigenvalue  $T_{\min}$  that remains strictly positive. This indicates that no wavefront is fully reflected by the scattering medium. The precise value of  $T_{\min}$  depends on the transverse width W, with  $T_{\min} \to 0$  as  $W \to \infty$ . This is because the number of propagating channels, which travel along distances  $L'_n = L/\sqrt{1-(n\pi/kW)^2}$ , increases as W grows, leading to more channels for which  $L'_n > \ell(\omega)$ . We note that there is no theoretical prediction available to accurately describe P(T) for  $L \lesssim \ell(\omega)$ . In particular, the prediction from the Dorokhov-Mello-Peyrera-Kumar (DMPK) equation is inaccurate (result not shown) because it relies on the assumption of scattering channel isotropy [36,39,40], which does not hold in the quasiballistic regime.

As  $\omega$  progressively approaches  $\omega_0$  ( $\delta = 8$ ), light and matter increasingly couple, and the transport mean free path decreases. As a consequence, transmission eigenchannels cover the full range  $T \in [0, 1]$ , with a distribution P(T) that

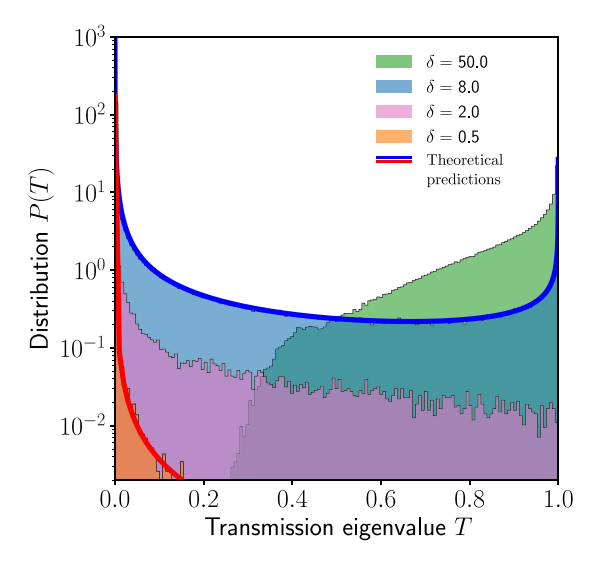


FIG. 2. Probability distribution of the eigenvalues  $T_n$  of the matrix  $\mathbf{t}^\dagger(\omega)\mathbf{t}(\omega)$ . Different histograms correspond to different detuning values  $\delta=2(\omega-\omega_0)/\Gamma_0$ , and therefore to different mean free paths (see Table I for reference). The solid blue line is the analytical prediction in the diffusive regime given by Eqs. (14)–(16). The solid red line corresponds to the analytical prediction in the localized regime, given by Eqs. (17) and (18), where  $\xi=N\pi\ell(\omega)/2$  with  $\ell(\omega)$  given by Eq. (14). All distributions are computed for 5760 disorder configurations with  $N_s=2\times 10^4$  scatterers, with a quality factor  $Q=\omega_0/(\Gamma_0/2)=10^3$  in a waveguide of longitudinal size  $k_0L=5000$  and of transverse size  $k_0W=161$ . The number of modes (which increases with the detuning) is N=53 in the quasiballistic regime and N=51 in the other regimes.

develops a second peak at T=0 (shaded blue in Fig. 2). In the diffusive regime  $\ell(\omega) \ll L \ll \xi$ , the average transmission eigenvalue,  $\langle T(\omega) \rangle = \langle \text{Tr}[\mathbf{t}(\omega)^{\dagger}\mathbf{t}(\omega)] \rangle / N$ , follows from the result of the diffusion equation for the mean intensity of light [34],

$$\langle T(\omega) \rangle = \frac{\pi \ell(\omega)/2}{L + \pi \ell(\omega)/2},$$
 (15)

and the distribution P(T) is very well described by the bimodal prediction [36,39]

$$P(T) = \frac{\langle T(\omega) \rangle}{2T\sqrt{1-T}},\tag{16}$$

which supports a finite number  $g=N\langle T(\omega)\rangle\gg 1$  of open channels with transmission close to unity [41], whereas the medium is opaque for random wavefronts and plane waves  $(\langle T(\omega)\rangle\ll 1)$ . The blue solid line in Fig. 2 corresponds to the prediction given by Eqs. (14)–(16). Since the result in Eq. (16) can be derived using the DMPK approach—a scaling analysis of transmission that presumes a characteristic length scale,  $\ell(\omega)$ , linked to a linearly inverse decrease in conductance with system size—it is unsurprising that this result holds for the resonant media considered here, provided that  $\ell(\omega)$  is appropriately calculated.

When the localization length equals the system length  $(\delta = 2)$ , the number of open channels reduces to  $g \simeq 1$ , causing the distribution P(T) to lose its peak at T = 1 (shown in pink in Fig. 2). At  $\delta = 0.5$ , where  $\xi \ll L$ , most transmission eigenvalues approach zero (see orange histogram in Fig. 2). More specifically, for each realization of disorder, all eigenvalues  $T_n$  are much smaller than the largest one. Consequently, the eigenvalue distribution takes the form

$$P(T) \simeq \frac{N-1}{N} \delta(T) + \frac{1}{N} P_{\text{max}}(T), \tag{17}$$

where  $P_{\rm max}(T)$  is the distribution of  $T_{\rm max}={\rm max}(T_n)$ . The largest eigenvalue, which exhibits significant fluctuations, follows an approximately log-normal distribution with  ${\rm Var}[\ln(T_{\rm max})]=-2\langle\ln(T_{\rm max})\rangle=4L/\xi\gg 1$ . Its distribution can be closely approximated by

$$P_{\max}(T) = C(\xi) \sqrt{\ln\left(\frac{4}{T}\right)} \frac{e^{-\frac{\xi}{2L}\left[\frac{\ln(T/4)}{2} + \frac{L}{\xi}\right]^2}}{T},$$
 (18)

where  $C(\xi)$  is a normalization factor that depends on  $\xi$ . This expression is obtained from Refs. [42,43] in the limit of vanishing conductance g. The distribution P(T) given by Eqs. (17) and (18) is in very good agreement with our numerical results (red solid line in Fig. 2). It implies in particular

that

$$\langle T \rangle \simeq \kappa \frac{e^{-L/2\xi}}{N} \ll \langle T_{\rm max} \rangle \simeq \kappa e^{-L/2\xi} \ll {\rm max}(T_{\rm max}) \simeq 1,$$

where  $\kappa = C(\xi)[2\sqrt{\pi}\operatorname{erfc}(\ln(4)^{1/2}) + \ln 4]$ , with erfc the complementary error function. For a finite number N<sub>r</sub> of disorder realizations, a rough estimate of the largest accessible eigenvalue,  $T_{\rm M}={\rm max}(T_{\rm max})$ , is given by the solution of  $NN_r \int_{T_{\rm M}}^1 {\rm d}T P(T) = 1$ . In the simulations at  $\delta = 0.5$  presented in Fig. 2, where  $L/\xi = 5$ , N = 51, and  $N_r = 5760$ , we find  $\langle T \rangle \simeq 1.3 \times 10^{-4}$ ,  $\langle T_{\rm max} \rangle \simeq 7 \times 10^{-3}$ , and  $T_{\rm M} \simeq 0.2$ . This shows that the use of wavefront shaping can lead to orders-of-magnitude enhancement in transmission, transitioning from an incident plane wave—which typically exhibits a transmission comparable to the mean transmission  $\langle T \rangle$ —to the maximally transmitted eigenchannel.

#### C. Eigenstate propagation

The eigenstates of  $\mathbf{t}(\omega)^{\dagger}\mathbf{t}(\omega)$  are of the form  $V_n(x,y) = \sum_{p=1}^N c_p^{(n)} \sqrt{k/k_p} e^{ik_p x} \xi_p(y)$ , with  $\sum_{p=1}^N |c_p^{(n)}|^2 = 1$ . The fields  $\Psi_n(\mathbf{r})$  resulting from their propagation through the disordered system are obtained by solving the coupled dipole equations,

$$\Psi_n(\mathbf{r}) = V_n(\mathbf{r}) - k^2 \sum_{i=1}^{N_s} \tilde{G}_0(\mathbf{r}, \mathbf{r}_i, \omega) \tilde{\alpha}(\mathbf{r}_i, \omega) \tilde{\psi}_i, \qquad (19)$$

$$\Psi_{n}(\mathbf{r}) = V_{n}(\mathbf{r}) - k^{2} \sum_{i=1}^{N_{s}} \tilde{G}_{0}(\mathbf{r}, \mathbf{r}_{i}, \omega) \tilde{\alpha}(\mathbf{r}_{i}, \omega) \tilde{\psi}_{i}, \qquad (19)$$

$$\tilde{\psi}_{i} = V_{n}(\mathbf{r}) - k^{2} \sum_{\substack{j=1\\j\neq i}}^{N_{s}} \tilde{G}_{0}(\mathbf{r}_{i}, \mathbf{r}_{j}, \omega) \tilde{\alpha}(\mathbf{r}_{j}, \omega) \tilde{\psi}_{j}. \qquad (20)$$

Figure 3 displays the intensity patterns  $I_n(x, y) = |\Psi_n(x, y)|^2$ and the corresponding integrated intensity profiles  $I_n(x) =$  $\int_0^W dy I_n(x, y)$ , shown for both the diffusive (top row) and localized (bottom row) regimes. Typical input states  $V_n$  are illustrated for low transmission in the left column and high transmission in the right column. To improve clarity, these simulations are conducted for square systems ( $k_0W = k_0L =$ 60). In each regime, however, the detuning is adjusted so that the distribution of transmission eigenvalues qualitatively resembles that in Fig. 2, in the diffusive (blue histogram) and localized (orange histogram) regimes.

In the diffusive regime, the intensity maps  $I_n(x, y)$  are statistically invariant along the y direction (Fig. 3, top), with a profile  $\langle I_n(x) \rangle$  that depends on the eigenvalue  $T_n$ . The most open channels  $(T_n \simeq 1)$  have a symmetric bell shape [blue dashed line in Fig. 3(b)], whose maximum increases linearly with the optical thickness  $L/\ell(\omega)$ , in agreement with experimental and numerical observations for nonresonant media [2,44,45]. For  $L \gg \ell(\omega)$ , their profile is well captured by the formula

$$\langle I_{T=1}(x)\rangle \simeq \frac{2\langle I_{T=1}(0)\rangle}{\pi\langle T(\omega)\rangle} \sin\left[\pi \frac{x+z_0(\omega)}{L+2z_0(\omega)}\right],$$
 (21)

where  $\langle I_{T=1}(0)\rangle = \langle \sum_{p=1}^{N} |c_p^{(n=1)}|^2 k/k_p \rangle \gtrsim 1$  and  $z_0(\omega) = \pi \ell(\omega)/4$  is the extrapolation length [46]. On the other hand, by extrapolating the results of Ref. [44] at small transmission, we find that closed channels  $(T_n \ll 1)$  are expected to decay exponentially as

$$\langle I_{T_n \ll 1}(x) \rangle \simeq 2 \langle I_{T=1}(x) \rangle e^{-2x/\xi_n},$$
 (22)

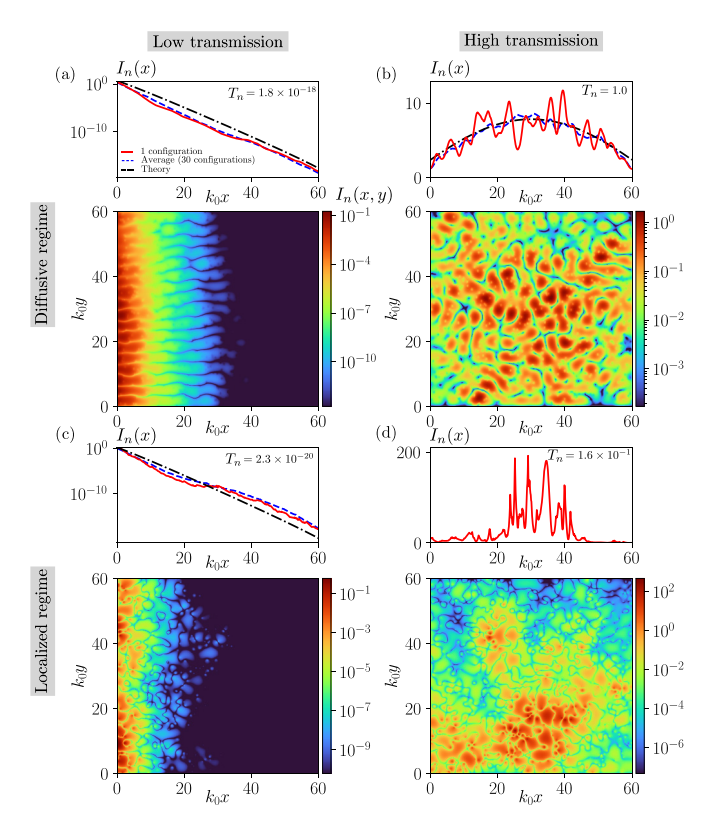


FIG. 3. Intensity maps  $I_n(x,y) = |\Psi_n(x,y)|^2$  (in units of  $k_0$ ) and integrated intensity profiles  $I_n(x) = \int_0^W \mathrm{d}y I_n(x,y)$  for typical incident wavefronts, chosen as different eigenstates  $V_n$  of the matrix  $\mathbf{t}^{\dagger}(\omega)\mathbf{t}(\omega)$ , in both the diffusive (first row) and localized regimes (second row). The left (right) column corresponds to the propagation of a low (high) transmission eigenstate in each regime. For clarity, the results correspond to square systems with  $k_0L = k_0W = 60$ ,  $N_s = 960$ , and  $Q = 10^3$ . In each regime, detuning is adjusted so that the distribution of transmission eigenvalues qualitatively resembles Fig. 2:  $\delta = 3$ , yielding  $k\ell(\delta = 3) \simeq 9.4$  in the diffusive regime and  $\delta = 0$  yielding  $k\ell(\delta = 0) \simeq 1.0$  in the localized regime. The solid red lines in  $I_n(x)$  represent the specific disorder realization associated with the intensity map below, while dashed blue lines show the average intensity over 30 disorder configurations. The dashed-dotted black lines in the diffusive regime correspond to Eqs. (14) and (21) for the open channel and to Eq. (22) for the closed channels. In the localized regime, numerical results for closed channel profile  $\langle I_n(x) \rangle$ are compared with the exponential profile  $e^{-\ln(4/T_n)x/L}$ 

with  $\xi_n \simeq 2L/\ln(4/T_n)$ . This prediction is in qualitative agreement with our results for resonant media [black dash-dotted line in Fig. 3(a)]. Both results (21) and (22) drastically differ from the linear decay of plane wave propagation,  $\langle I(x)\rangle \propto$ (L-x)/L, imposed by conservation of the mean current.

In the localized regime, the intensity maps  $I_n(x, y)$  exhibit significant fluctuations. Notably, the states associated with the largest transmission eigenvalues lose their invariance along the y direction [see Fig. 3(d)]. Each of these states arises from the efficient excitation of a cluster of a few exponentially localized quasinormal eigenmodes of the system [47,48], enabling light to percolate through to the transmission side, with transmission potentially orders of magnitude larger than the transmission of a simple plane wave. The intensity of these states inside the medium can also be much larger than the intensity of the open channels found in the diffusive regime (compare the intensity values in the two maps on the right). This could be attributed to a difference in the value of  $\ell(\omega)$  in both scenarios. The vast majority of the transmission eigenstates present, however, a very low transmission. The corresponding intensity profiles  $I_n(y)$  decay exponentially within the medium [see Fig. 3(c)], with localization lengths  $\xi_n \simeq n(\pi/2)\ell(\omega)$  related to the transmission by  $T_n = 4e^{-2L/\xi_n}$  [36], similar to the behavior observed for closed channels in the diffusive regime [see Eq. (22)].

# III. DWELL-TIME OPERATOR AND RADIATION TRAPPING

#### A. Electromagnetic energy and the dwell-time operator

To establish the expression of a dwell-time operator in a resonant medium, it is useful to formally write the coupled dipole equations (1) and (2) as a wave equation,  $[\nabla^2 + k^2 \varepsilon(\mathbf{r}, \omega) + i0^+] G(\mathbf{r}, \mathbf{r}', \omega) = \delta(\mathbf{r} - \mathbf{r}')$ . By noting that the exciting fields  $\tilde{\psi}_i$  in Eq. (2) can be written as  $\tilde{\psi}_i = G(\mathbf{r}_i, \mathbf{r}', \omega)/[1 - k^2 \tilde{G}_0(\mathbf{r}_i, \mathbf{r}_i, \omega)\tilde{\alpha}(\mathbf{r}_i, \omega)]$ , we find that  $G(\mathbf{r}, \mathbf{r}', \omega)$  in Eq. (1) obeys a wave equation with a frequency-dependent dielectric constant of the form

$$\varepsilon(\mathbf{r},\omega) = 1 + \sum_{i=1}^{N_s} \frac{\tilde{\alpha}(\mathbf{r}_i,\omega)}{1 - k^2 \tilde{G}_0(\mathbf{r},\mathbf{r}_i,\omega) \tilde{\alpha}(\mathbf{r}_i,\omega)} \delta(\mathbf{r} - \mathbf{r}_i),$$
(23)

which satisfies  $\operatorname{Im}[\varepsilon(\mathbf{r},\omega)] = 0$ , although  $\operatorname{Re}[\tilde{G}_0(\mathbf{r}_i,\mathbf{r}_i,\omega)]$  diverges, since  $\operatorname{Im}[1/\tilde{\alpha}(\mathbf{r}_i,\omega)] = k^2 \operatorname{Im}[\tilde{G}_0(\mathbf{r}_i,\mathbf{r}_i,\omega)]$  in the absence of absorption. Here,  $\varepsilon(\mathbf{r},\omega)$  should be regarded as a formally defined quantity, and not as the relative dielectric permittivity associated with a macroscopic displacement field. For such nonabsorbing medium, the local electromagnetic energy density, associated with an arbitrary field  $\psi(\mathbf{r},\omega)$  solution of the wave equation, is [49]

$$u(\mathbf{r},\omega) = \frac{\varepsilon_0}{4\omega} \partial_{\omega} [\omega^2 \varepsilon(\mathbf{r},\omega)] |\psi(\mathbf{r},\omega)|^2.$$
 (24)

In Ref. [15], it was demonstrated that the total energy within the scattering region V, given by  $U(\omega) = \int_{V} d\mathbf{r} u(\mathbf{r}, \omega)$ , where  $u(\mathbf{r}, \omega)$  takes the form of Eq. (24), can be expressed in terms of the so-called dwell-time operator  $\mathbf{Q}_d(\omega)$ ,

$$U(\omega) = \phi_{\rm in} \langle \psi_{\rm in} | \mathbf{Q}_d(\omega) | \psi_{\rm in} \rangle. \tag{25}$$

Here,  $\phi_{\rm in}$  is the power carried by the incoming field  $|\psi_{\rm in}\rangle$ , normalized such that  $\langle\psi_{\rm in}|\psi_{\rm in}\rangle=1$  (the original incident field must be multiplied by  $\sqrt{\varepsilon_0c/2\phi_{\rm in}}$  to get  $\psi_{\rm in}$ ). Equation (25) shows that  $\tau(\omega)=U(\omega)/\phi_{\rm in}=\langle\psi_{\rm in}|{\bf Q}_d(\omega)|\psi_{\rm in}\rangle$  represents the dwell time of the field inside the scattering region when illuminated with the wavefront  $|\psi_{\rm in}\rangle$ .

Focusing on the case where  $|\psi_{\rm in}\rangle$  propagates from left to right (see Fig. 1) and contains no evanescent components,  $|\psi_{\rm in}\rangle$  can be represented in the basis of the *N* propagating channels. The  $N \times N$  dwell-time operator takes the form [15]

$$\mathbf{Q}_d(\omega) = \mathbf{Q}(\omega) + \mathbf{Q}_i(\omega) + \mathbf{Q}_e(\omega), \tag{26}$$

where  $\mathbf{Q}(\omega)$  is the Wigner-Smith operator [50,51],

$$\mathbf{Q}(\omega) = -i[\mathbf{t}(\omega)^{\dagger} \partial_{\omega} \mathbf{t}(\omega) + \mathbf{r}(\omega)^{\dagger} \partial_{\omega} \mathbf{r}(\omega)]. \tag{27}$$

For standard input wavefronts  $|\psi_{\rm in}\rangle$ , such as plane waves close to normal incidence,  ${\bf Q}(\omega)$  is responsible for the largest contribution to the dwell time. The Wigner-Smith operator enables the multichannel generalization of the notion of time delay through a scattering potential. It gives information on the delay experienced by the central component of a wave packet propagating through the disordered sample [13]. The second term  ${\bf Q}_i(\omega)$  results from the interference of the incident and reflected fields. It reads

$$\mathbf{Q}_{i}(\omega) = -i\frac{\mathbf{D}(\omega)\mathbf{r}(\omega) - \mathbf{r}(\omega)^{\dagger}\mathbf{D}(\omega)}{2},$$
 (28)

where  $\mathbf{D}(\omega)$  is an  $N \times N$  diagonal matrix with elements  $D_{mm}(\omega) = \omega/[\omega^2 - (m\pi c/W)^2]$  ( $m \le N$ ). The contribution of  $\mathbf{Q}_i(\omega)$  is significant for states of low dwell time, which do not penetrate deeper than a few mean free paths inside the scattering volume. Finally,  $\mathbf{Q}_e(\omega)$  captures dwell-time contributions due to scattering into evanescent channels of the empty waveguide,

$$\mathbf{Q}_{e}(\omega) = \frac{\mathbf{t}_{e}(\omega)^{\dagger} \mathbf{D}_{e}(\omega) \mathbf{t}_{e}(\omega) + \mathbf{r}_{e}(\omega)^{\dagger} \mathbf{D}_{e}(\omega) \mathbf{r}_{e}(\omega)}{2}.$$
 (29)

Here,  $\mathbf{t}_e(\omega)$  and  $\mathbf{r}_e(\omega)$  are the transmission and reflection matrices that connect the N input propagation channels to  $N_e$  output evanescent channels; they are of size  $N_e \times N$  and take the same form as in Eqs. (7) and (8), except that  $k_m = ik\sqrt{(m\pi/kW)^2-1}$ , with  $N < m \le N_e + N$ . In addition,  $\mathbf{D}_e(\omega)$  is an  $N_e \times N_e$  diagonal matrix with elements  $D_{emm}(\omega) = \omega/[\omega^2 - (m\pi c/W)^2]$  ( $N < m \le N_e + N$ ). The contribution of  $\mathbf{Q}_e(\omega)$  to the dwell time is negligible, except when the transverse system size causes a geometrical resonance due to the birth of a new propagating mode, i.e., when kW is close to a  $\pi$ -integer.

#### B. Dwell-time eigenvalue distribution

The dwell-time eigenvalue distribution is defined as

$$P(\tau) = \frac{1}{N} \left\langle \sum_{n=1}^{N} \delta(\tau - \tau_n) \right\rangle, \tag{30}$$

where  $\tau_n$  are the eigenvalues of the matrix  $\mathbf{Q}_d(\omega)$  introduced in Eq. (26). This distribution is shown in Fig. 4 for different detuning values  $\delta$ , while keeping all other parameters (the waveguide length L, width W, number of resonators  $N_s$ , and quality factor Q) fixed. To facilitate comparison between the results for  $P(\tau)$  and P(T), these parameters are identical to those used in Fig. 2.

In the quasiballistic regime ( $\delta = 50$ , green histogram in Fig. 4), the distribution  $P(\tau)$  reflects the dispersion of the channels of the empty waveguide. The dwell time of channel n of the waveguide is simply  $\tau_n = \tau_b/\sqrt{1 - (n\pi/kW)^2}$ , with  $\tau_b = L/c$  the ballistic time for straight propagation along the waveguide axis. In the limit of a large number of propagation channels,  $N = \lfloor kW/\pi \rfloor \gg 1$ , we deduce the following distribution of normalized dwell time  $\tilde{\tau} = \tau/\tau_b$ :

$$P(\tilde{\tau}) = \frac{1}{\tilde{\tau}^2 \sqrt{\tilde{\tau}^2 - 1}}.\tag{31}$$

This simple prediction appears in good agreement with simulations, provided a scaling factor is introduced to account for

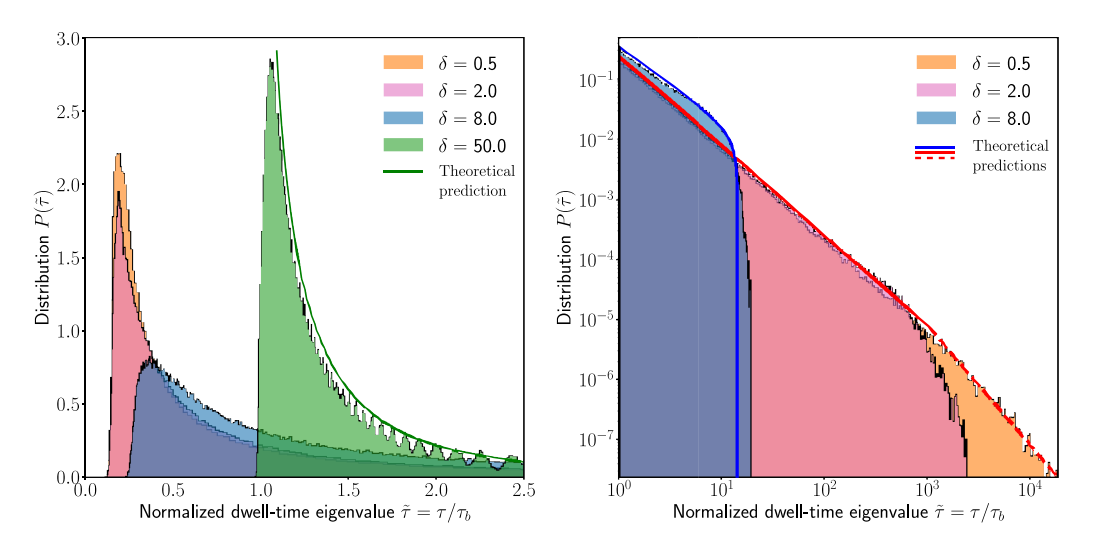


FIG. 4. Probability distribution of the eigenvalues  $\tau_n$  of the dwell-time operator  $\mathbf{Q}_d$ . Different histograms correspond to varying detuning values  $\delta$ , with system dimensions and density matching those used in Fig. 2 (see Table I for details on the propagation regimes). The left panel displays the short-time histograms on a linear scale, while the right panel shows the long-time tails on a log-log scale. The solid green line is a theoretical prediction based on the ballistic time of rays in the sample, as expressed in Eq. (31), multiplied by a 1.5 scaling factor. The solid blue line represents the theoretical prediction for the diffusive regime, as described by the combination of Eqs. (14), (32), (33), and (34). The solid and dotted red lines correspond to Eqs. (36) and (37), respectively. All times are normalized by the ballistic time,  $\tau_b = L/c$ .

the residual scattering at short dwell time (green solid line in Fig. 4). In the tail of the distribution, the spacing between successive  $\tau_n$  becomes larger than the disorder-induced fluctuations around each  $\tau_n$  value, revealing the underlying discrete nature of the channels in  $P(\tilde{\tau})$ . This effect disappears as W increases (result not shown).

In the diffusive regime ( $\delta=8$ ), the distribution  $P(\tilde{\tau})$  broadens, with a minimum at  $\tau\ll\tau_b$  (Fig. 4, left) and a tail extending to large times  $\tau\gg\tau_b$  (Fig. 4, right). The eigenstates associated with short dwell times correspond to reflected wavefronts, while those with long dwell times correspond to transmitted wavefronts. In Ref. [15], it is proven that the distribution  $P(\tilde{\tau})$  of nonresonant diffusive media takes the form

$$P(\tilde{\tau}) = \frac{2\tau_s}{\pi \tau_b} \frac{1}{\tilde{\tau}^2} \sqrt{(\alpha \tilde{\tau} - 1)(1 - \beta \tilde{\tau})} (1 + \gamma \tilde{\tau}). \tag{32}$$

Here,  $\tau_s$  is the scattering time (which expression will be given later), and  $\alpha$ ,  $\beta$ , and  $\gamma$  are coefficients that depend on  $\tau_s/\tau_b$  and  $\tau_s/\langle \tau \rangle$ , where  $\langle \tau \rangle$  is the mean dwell time. Defining  $X = \sqrt{\beta/\alpha}$ , these coefficient are solutions of  $(1-X)^2(3+2X+2X^2)/[2X(1+X^2)] = \langle \tau \rangle/\tau_s$ ,  $\alpha = (\tau_b/\tau_s)(1+X)/(1-X^2)^2$  and  $\gamma = 2(\tau_b/\tau_s)X^2/(1-X^2)^2$ . In the regime of large optical thickness, the distribution (32) predicts that nonzero eigenvalues lie in the interval  $\tau_s \lesssim \tau \lesssim 4\langle \tau \rangle^2/9\tau_s$ , and that the maximum of the distribution is reached for  $\tau \simeq 4\tau_s/3$ .

In nonresonant disordered media, the scattering time and mean time are given by  $\tau_s = (\pi/2)\ell/v_{\varphi}$  and  $\langle \tau \rangle = (\pi/2)L/v_{\varphi}$ , where  $v_{\varphi} = c/n$  is the phase velocity, n being the real part of the effective refractive index experienced by the mean field [15]. This implies that the largest accessible dwell time is  $\tau_{\rm max} = (2\pi/9)L^2/\ell v_{\varphi} = (\pi^3/9)\tau_{\rm Th}$ , where  $\tau_{\rm Th} = L^2/\pi^2 D_B$  is the Thouless time. Here,  $D_B = \ell v_E/2$  is the diffusion coefficient of the mean intensity, with  $v_E = v_{\varphi}$ 

for nonresonant media, and  $\tau_{Th}$  is the longest mode lifetime of the corresponding diffusion equation.

It is worth noting that the largest dwell time  $\tau_{max} \sim \tau_{Th}$  is significantly greater than the dwell time  $\tau_{PW}$  associated with a plane wave or a random wavefront, as the latter scales with the average dwell time  $\langle \tau \rangle$  [15]. This difference arises because  $\tau_{PW}$  is essentially the product of the transmission diffusive time  $\tau_{Th}$  and the probability  $\sim \!\! \ell/L$  of reaching the transmission side. Wavefront shaping allows an increase in the transmission probability, resulting in  $\tau_{max}/\tau_{PW} \sim L/\ell \gg 1$ . Notably, this property is also preserved in resonant materials, as we shall see.

In resonant disordered media, the energy velocity  $v_E$  is strongly reduced near resonance, as light can spend a time of order  $\Gamma_0^{-1}$  inside each resonator between two scattering events separated by a distance  $\ell(\omega)$ . By adapting expressions found in Ref. [30] to the case of 2D scattering, we find that, in the dilute regime  $k_0 a \gg 1$ , with  $a = (N_s/WL)^{-1/2}$  the mean distance between scatterers, the energy velocity is given by

$$\frac{1}{v_F(\omega)} = \frac{v_\varphi}{c^2} + \frac{1}{\Gamma_0 \ell(\omega)} \left( 1 + \frac{2}{\pi O} \right),\tag{33}$$

for  $\delta \ll Q$ , where  $v_{\varphi} \simeq c(1+2\delta/[(k_0a)^2(\delta^2+1)])$ . Consequently, both the Thouless time  $\tau_{\text{Th}}$  and the mean dwell time  $\langle \tau \rangle$  [52] are increased near resonance. Assuming that the scaling of  $\tau_{\text{max}}$  with  $\tau_{\text{Th}}$  must hold for resonant media, we find that the scattering time and mean time are given by

$$\tau_s = \frac{\pi}{2} \frac{\ell(\omega)}{v_E(\omega)} \quad \text{and} \quad \langle \tau \rangle = \frac{\pi}{2} \frac{L}{v_E(\omega)}.$$
(34)

Very good agreement is observed in the diffusive regime between the prediction for  $P(\tilde{\tau})$  given by Eqs. (32)–(34) with the above parameters and the simulation results (solid blue line in Fig. 4, right).

An interesting result of energy velocity modulation is the potential to significantly increase the maximum accessible

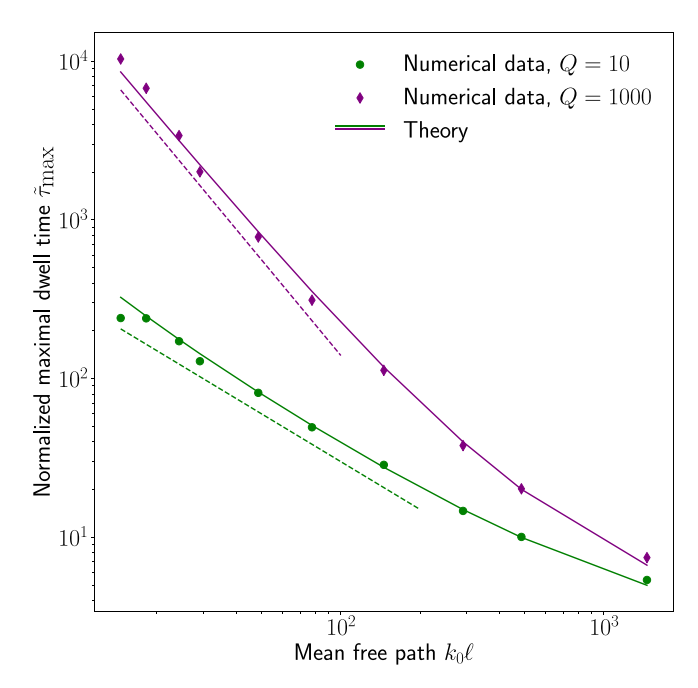


FIG. 5. Maximal dwell time in the diffusive regime for moderate (green) and large (purple) values of the quality factor Q of the resonators. The normalized mean free path  $k_0\ell(\omega)$ , given by Eq. (14), is tuned by varying the number of scatterers from  $N_s=100$  to 12750, while keeping the frequency on resonance ( $\delta=0$ ). The system has length  $k_0L=5000$  and supports N=47 transverse channels. Numerical simulation results (dots) are compared to the theoretical prediction (solid lines), determined by the upper edge  $1/\beta$  of the distribution (32), with a good approximation provided by Eq. (35). Dotted lines highlight the  $1/\ell(\omega)$  dependence of the maximal dwell time when  $Q\ll 2k_0\ell(\omega)$  and the  $1/\ell(\omega)^2$  dependence when  $Q\gg 2k_0\ell(\omega)$ .

dwell time by enhancing the quality factor Q of the resonators. To demonstrate this, we represent in Fig. 5 the largest normalized dwell time  $\tilde{\tau}_{\max} = \tau_{\max}/\tau_b$  computed at resonance ( $\delta=0$ ) as a function of disorder strength, for both low and high Q resonators. The disorder strength, quantified by  $k\ell(\omega)$ , is modified by varying the number of scatterers  $N_s$ , while fixing the system size. Apart from the excellent agreement between simulations and theory, we find that the dwell time in high-Q systems can be enhanced by a factor of  $\sim Q/2k\ell(\omega)$  compared to low-Q systems, potentially leading to high radiation trapping effect. Indeed, by considering the limit  $L\gg\ell(\omega)$  in Eq. (32) and neglecting the small impact of the refractive index on phase velocity, we find that the largest normalized dwell time  $\tilde{\tau}_{\max} = \tau_{\max}/\tau_b$  is given by

$$\tilde{\tau}_{\text{max}} \simeq \frac{2\pi}{9} \frac{L}{\ell(\omega)} \left[ 1 + \frac{Q}{2k\ell(\omega)} \right].$$
 (35)

Whereas  $\tilde{\tau}_{\text{max}}$  scales as  $1/\ell(\omega)$  for low-Q systems, it scales as  $Q/\ell(\omega)^2$  for high-Q systems (see dashed line in Fig. 5).

Figure 4 also presents results for  $P(\tilde{\tau})$  in the localized regime  $\xi \lesssim L$  ( $\delta = 0.5$ , orange histograms). In this regime, we must distinguish between states that explore a region smaller than the localization length  $\xi$  before escaping and those that stay longer and are affected by the localization process. For  $\tau \lesssim \xi^2/D_B \sim N^2 \tau_s$ , the states explore the system diffusively.

Taking the limit  $L \to \infty$  in Eq. (32), we obtain  $\alpha = 1$ ,  $\beta = 0$ , and  $\gamma = 0$ , yielding

$$P(\tau) = \frac{2\tau_s}{\pi} \frac{1}{\tau^2} \sqrt{\frac{\tau}{\tau_s} - 1} \quad \text{for} \quad \tau \lesssim N^2 \tau_s.$$
 (36)

This prediction is shown as a solid red line in Fig. 4, right. For  $\tau \gtrsim N^2 \tau_s$ , the distribution  $P(\tau)$  can be derived by noting that the longest dwell time corresponds to the Wigner time in the localized regime,  $\tau_W = \sum_{n=1}^N \tau_n \simeq \max(\tau_n)$ . By extrapolating known results for the Wigner time in nonresonant media [53–55] to resonant cases, we find

$$P(\tau) = \frac{(\pi/2)N\ell(\omega)}{v_E(\omega)\tau^2} \quad \text{for} \quad \tau \gtrsim N^2 \tau_s, \tag{37}$$

which becomes frequency-independent for high-Q systems,  $P(\tau) \simeq (\pi/2)N/\Gamma_0\tau^2$ . Up to a prefactor, Eq. (37) aligns with the prediction of Ref. [56], which investigates  $P(\tau)$  for non-resonant wave scattering, with waves injected from both sides of the medium. The robustness of the power-law scaling in  $P(\tau)$  originates from the distribution of decay rates  $\Gamma$  of the quasimodes in localized disordered systems [53,57]. By connecting the Wigner time and the density of quasimodes, we find that  $\int_{\tau} \mathrm{d}\tau' P(\tau') \propto N\langle\tau\rangle \int^{1/\tau} \mathrm{d}\Gamma \, \Gamma P(\Gamma)$ , leading to  $P(\tau) \sim 1/\tau^2$  because  $P(\Gamma) \sim 1/\Gamma$  in any dimension within the localized regime [57]. The prediction (37) is shown as a dashed red line in Fig. 4, right.

### C. Eigenstate propagation

According to Eq. (25), if the incident wavefront  $|\psi_{\rm in}\rangle$  is chosen as an eigenstate of  $\mathbf{Q}_d(\omega)$  with eigenvalue  $\tau$ , it will deposit the electromagnetic energy  $U(\omega) = \phi_{\rm in}\tau$  inside the medium. In this sense, the eigenstates of  $\mathbf{Q}_d(\omega)$  correspond to incident wavefronts optimized for maximizing the total stored energy. We refer to these as radiation trapping eigenstates. Wavefront shaping can thus be applied to the dwell time operator  $\mathbf{Q}_d(\omega)$  in the same way as for the transmission matrix  $\mathbf{t}^{\dagger}(\omega)\mathbf{t}(\omega)$ .

In a symmetric manner to Fig. 3, we present in Fig. 6 typical intensity maps corresponding to the propagation of various eigenvectors of the dwell-time operator  $\mathbf{Q}_d(\omega)$ . These maps are obtained by solving the coupled dipole equations (19) and (20), where  $V_n(\mathbf{r})$  now represents a dwell-time eigenstate. To facilitate comparison with the intensity maps of transmission eigenstates, the system parameters  $(k_0W, k_0L, N_s, \delta, Q)$  are identical to those in Fig. 3. This implies that the distribution of dwell-time eigenvalues (not shown) qualitatively resembles that in Fig. 4 for the diffusive (blue histogram) and localized (orange histogram) regimes, but with a larger normalized scattering time  $\tau_s/\tau_b \simeq (\pi/4)Q/kL \simeq 13$ , since the shorter system length  $(k_0L=60)$  instead of  $k_0L=5000$ ) reduces the value of  $\tau_b=L/c$ .

The left column of Fig. 6 shows states with dwell times similar to the mean dwell time in the diffusive regime,  $\langle \tau \rangle / \tau_b \simeq (\pi/4) Q/k \ell(\omega) \simeq \pi Q/[(1+\delta^2)(ka)^2] \simeq 84$  at  $\delta = 3$ , yet significantly longer than the scattering time, which corresponds to the most probable time in the diffusive regime,  $4\tau_s/3\tau_b \simeq 17$ . Conversely, the right column of Fig. 6 shows states with dwell times close to the largest accessible values, in both the diffusive and localized regimes. In the

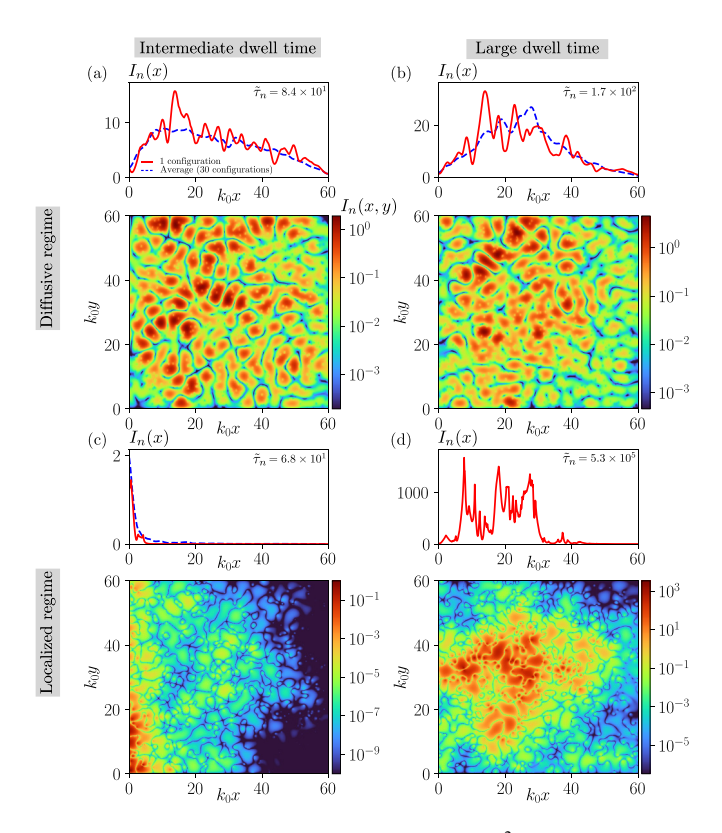


FIG. 6. Intensity maps  $I_n(x,y) = |\Psi_n(x,y)|^2$  (in units of  $k_0$ ) and integrated intensity profiles  $I_n(x) = \int_0^W \mathrm{d}y I_n(x,y)$  for typical incident wavefronts, chosen as different eigenstates  $V_n$  of the matrix  $\mathbf{Q}_d(\omega)$ , in both the diffusive (first row,  $k\ell(\delta=3)\simeq 9.4$ ) and localized regimes (second row,  $k\ell(\delta=0)\simeq 1.0$ ). System dimensions  $(k_0W, k_0L)$  and resonator characteristics  $(\delta, Q, N_s)$  match those used in Fig. 3. The left column corresponds to the propagation of eigenstates with dwell times  $\tau_n$  close to the mean time  $\langle \tau \rangle / \tau_b = (\pi/2)(\ell(\omega)/L)(c/v_E(\omega)) \simeq 84$  in the diffusive regime, while the right column shows eigenstates with  $\tau_n$  close to the largest dwell time accessible in both regimes (see text for details). The solid red lines in  $I_n(x)$  represent the specific disorder realization associated with the intensity map below, while the dashed blue lines show the average intensity over 30 disorder configurations.

diffusive regime, Eq. (35) gives  $\tau_{\text{max}}/\tau_b \simeq (\pi/9)QkL/[k\ell(\omega)]^2 \simeq (16\pi/9)QkL/[(1+\delta^2)^2(ka)^4] \simeq 2 \times 10^2$  at  $\delta = 3$ . In the localized regime, a rough estimate of the accessible  $\tau_{\text{max}}$  using  $N_r$  disorder configurations is the solution of  $NN_r \int_{\tau_{\text{max}}}^{\infty} d\tau P(\tau) = 1$ , with  $P(\tau)$  given by Eq. (37). This gives  $\tau_{\text{max}}/\tau_b \simeq (\pi/4)QN^2N_r/kL \simeq 5 \times 10^5$  for  $N_r = 100$ .

In the diffusive regime (Fig. 6, upper row), dwell-time eigenstates are statistically invariant along the transverse direction, but the profile  $\langle I_n(x)\rangle = \int_0^W \mathrm{d}y \, \langle I_n(x,y)\rangle$  depends on the eigenvalue  $\tau_n$ . Generally, the larger  $\tau_n$ , the deeper the penetration of  $I_n(x)$  into the material. This property, which is apparent in nonresonant media, is less straightforward in resonant media because, according to the definition (25) of  $\mathbf{Q}_d$ , the normalized eigenvalue  $\tilde{\tau}_n = \tau_n/\tau_b$  is related to the field  $\Psi_n(\mathbf{r},\omega)$  by

$$\tilde{\tau}_n = \int_{\mathcal{V}} \frac{d\mathbf{r}}{L} \frac{\partial_{\omega} [\omega^2 \varepsilon(\mathbf{r}, \omega)]}{2\omega} |\Psi_n(\mathbf{r}, \omega)|^2, \tag{38}$$

which differs in a nontrivial way from the nonresonant result  $(c/v_{\varphi})\int_0^L dx \, I_n(x)/L$ . In particular, the values of  $\tilde{\tau}_n$  are much larger than the typical values of  $I_n(x)$  because most of the energy is stored inside the material degrees of freedom instead of the field. However, the profiles found for  $\langle I_n(x) \rangle$  are consistent with those for nonresonant media, as reported in Ref. [15]. As  $\tau_n$  increases,  $\langle I_n(x) \rangle$  evolves from an exponential profile near the injection surface to a profile that deposits most of the intensity within the bulk of the disordered system. The maximum dwell-time eigenstates [Fig. 3(b)] exhibit a peak intensity that is slightly shifted to the left of the sample midpoint x = L/2, due to the asymmetry induced by left-side injection, which breaks the system's statistical mirror symmetry. This symmetry can be restored by injecting light from both sides [15]. Although no theoretical prediction exists for  $\langle I_n(x) \rangle$ , we find that the profiles are qualitatively similar to those associated with transmission eigenchannels, showing slightly more intensity inside the sample for the largest dwell-time eigenstates than for the open channels [compare Fig. 3(b) with Fig. 6(b)].

In the localized regime (Fig. 6, lower row), eigenstates with dwell times similar to the mean diffusive dwell-time exhibit behavior quite distinct from that of corresponding diffusive states [compare Figs. 6(a) and 6(c)]. Notably, the intensity profile  $\langle I_n(x) \rangle$  is significantly more localized near the injection surface, suggesting that there is not always a straightforward relationship between the dwell time, as defined in Eq. (38), and the integrated intensity. In contrast, wavefronts with dwell time  $\tau \gg N^2 \tau_s$  produce intensity maps that are exponentially localized within the sample [Fig. 6(d)], indicating that they can efficiently couple to quasimodes deeply localized within the material. Interestingly, these states not only reach exceptionally large dwell times but also generate intensity patterns that are substantially more intense than those in the diffusive regime [compare Figs. 6(b) and 6(d)], and even surpass the intensity of the largest transmission eigenchannels in the localized regime [compare Fig. 3(d) with Fig. 6(d)]. This is because transmission eigenchannels optimize coupling between localized quasimodes to maximize transmission, whereas dwell-time eigenchannels optimize targeting the deepest and most isolated quasimodes.

### IV. CONCLUSION

In this work, we have shown that the transmission and dwell-time eigenvalue distributions of resonant disordered media, P(T) and  $P(\tau)$ , can be fully characterized by two mesoscopic parameters—the transport mean free path  $\ell(\omega)$  and the energy velocity  $v_E(\omega)$ —along with two geometric parameters, the system length L and the number of transverse channels N.

In the diffusive regime  $(\ell(\omega) \ll L \ll \xi)$ , P(T) follows the bimodal distribution (16), parameterized by the optical thickness  $L/\ell(\omega)$ , while  $P(\tau)$  follows Eq. (32), which is governed by both the optical thickness and the time between successive scattering events,  $\ell(\omega)/v_E(\omega)$ . In this regime, the use of wavefront shaping to synthesize eigenstates of either the transmission or the dwell-time operators enables transmission and energy storage that surpass those achievable with a plane wave or a random wavefront by a factor of  $L/\ell(\omega) \gg 1$ . Indeed,

 $\langle T \rangle \propto \ell(\omega)/L$  and  $T_{\rm max} \simeq 1$  yield  $T_{\rm max}/\langle T \rangle \propto L/\ell(\omega)$ , while  $\langle \tau \rangle \propto L/v_E(\omega)$  and  $\tau_{\rm max} \propto L^2/[\ell(\omega)v_E(\omega)]$  give  $\tau_{\rm max}/\langle \tau \rangle \propto L/\ell(\omega)$ . Additionally, using the explicit expression for the energy velocity, we demonstrated that  $\tau_{\rm max}$  can be enhanced by a factor  $c/v_E(\omega) \simeq Q/2k\ell(\omega) \gg 1$  when employing high-Q resonators instead of low-Q ones [see Eq. (35) and Fig. 5]. This contrasts with the portion of energy stored in the field, which scales as  $L/\ell(\omega)$  for both the open channels [Fig. 3(b)] and the eigenstates of  $\mathbf{Q}_d(\omega)$  associated with  $\tau_{\rm max}$  [Fig. 6(b)]. Notably, the field energy of the latter appears independent of the energy velocity and therefore independent of the quality factor of the resonators, at fixed detuning  $\delta$ .

In the localized regime  $(W < \xi \simeq (\pi/2)N\ell(\omega) < L)$ , the distributions P(T) and  $P(\tau)$  depend on an additional parameter: the number of channels N. Most transmission eigenvalues are close to zero, while the largest transmission eigenvalue typically follows a log-normal distribution [see Eq. (18)], exhibiting significant fluctuations  $[ln(T_{max})]$  has a standard deviation  $\propto \sqrt{L/\xi} \gg 1$ ]. This implies that a plane wave or a random wavefront typically yields a transmission  $\propto$  $e^{-2L/\xi}/N \ll 1$ , although specific disorder configurations can allow  $T_{\text{max}}$  to approach unity. The enhancement  $T_{\text{max}}/\langle T \rangle$ achieved through wavefront shaping is therefore even more pronounced than in the diffusive regime. The same applies to the control of energy storage via wavefront shaping. In contrast to the diffusive regime,  $P(\tau)$  remains unbounded in the localized regime [see Eq. (37)]. Since the mean time  $\langle \tau \rangle$  is proportional to the mean density of states and remains largely unaffected by localization, we find  $\tau_{\rm max}/\langle \tau \rangle \propto$  $N^2N_r\ell(\omega)/L\gg 1$ , where  $N_r$  is the number of disorder realizations probed. In addition, the advantage observed in the diffusive regime of working with high-Q resonators is preserved in the localized regime, as  $\tau_{max}$  remains proportional to  $c/v_E(\omega)$ .

Previous predictions apply to a wide range of two-dimensional disordered structures composed of resonant units, including thin metallic waveguides filled with sub-wavelength high-dielectric cylinders in the microwave domain [58–60], planar disordered waveguides [2,61], and more exotic nanostructures in the optical domain [62,63]. Moreover, since all our predictions for the diffusive regime are generically expressed in terms of the mean free path and the energy velocity—and since such a diffusive regime is also commonly observed in three-dimensional systems—we anticipate that our predictions will remain valid in three-dimensional diffusive systems composed of pointlike scatterers. This includes systems composed of resonant dielectric scatterers, cold atoms far from saturation, or artificial atoms, which can be accurately described using coupled-dipole equations [17,32].

An important aspect of energy storage in resonant media not addressed in this work is the detailed analysis of how energy is partitioned between the light and material degrees of freedom. While it is evident that high-Q systems store most of the energy within the material, it remains unclear to which degree this partitioning is influenced by factors such as disorder strength and the propagation regime (quasiballistic, diffusive, or localized). Additionally, it is unclear to which degree this partition can be controlled through wavefront shaping techniques. This issue will be explored in a forthcoming publication.

#### **ACKNOWLEDGMENTS**

This research has been supported by the ANR project MARS\_light under reference ANR-19-CE30-0026 and by the program "Investissements d'Avenir" launched by the French Government.

#### DATA AVAILABILITY

The data that support the findings of this study are available from the corresponding author upon reasonable request.

# APPENDIX A: COUPLED DIPOLE EQUATIONS IN A WAVEGUIDE

In this Appendix, we derive the coupled dipole equations for an assembly of resonant scattering dipoles in a waveguide. We consider the case of an incident z-polarized wave propagating through a two-dimensional waveguide embedded in the (x, y) plane. In this configuration, the scattering process preserves the polarization of the incident field, meaning all vector quantities are aligned with the  $\hat{\mathbf{z}}$  unit vector. For simplicity, we will omit vector notation and work exclusively with scalar quantities in the following derivation.

The scalar Green's function of the wave equation is given by

$$G(\mathbf{r}, \mathbf{r}', \omega) = \tilde{G}_0(\mathbf{r}, \mathbf{r}', \omega) - k^2 \alpha(\omega) \sum_{i=1}^{N_s} \tilde{G}_0(\mathbf{r}, \mathbf{r}_i, \omega) \psi_i,$$
(A1)

where  $\alpha(\omega)$  is the free space polarizability of a resonant scatterer and  $\tilde{G}_0(\mathbf{r}, \mathbf{r}', \omega)$  is the retarded Green's function of the wave equation in the empty waveguide with Dirichlet boundary conditions in the y direction, defined in Eq. (3). In addition, the field  $\psi_i$ , exciting the scatterer located at the position  $\mathbf{r}_i$ , includes the contribution of the source,  $\tilde{G}_0(\mathbf{r}_i, \mathbf{r}', \omega)$ , as well as the contributions of the different scatterers,

$$\psi_{i} = \tilde{G}_{0}(\mathbf{r}_{i}, \mathbf{r}', \omega) + \psi^{\circlearrowleft}(\mathbf{r}_{i}) - k^{2}\alpha(\omega) \sum_{\substack{j=1\\j\neq i}}^{N_{s}} \tilde{G}_{0}(\mathbf{r}_{i}, \mathbf{r}_{j}, \omega)\psi_{j}.$$
(A2)

Note, in particular, the radiation-reaction contribution from the scatterer i,

$$\psi^{\circlearrowleft}(\mathbf{r}_i) = -k^2 \Delta G_0(\mathbf{r}_i, \omega) \alpha(\omega) \psi_i, \tag{A3}$$

where  $\Delta G_0(\mathbf{r}_i, \omega) = \tilde{G}_0(\mathbf{r}_i, \mathbf{r}_i, \omega) - G_0(\mathbf{r}_i, \mathbf{r}_i, \omega)$ , and  $G_0(\mathbf{r}, \mathbf{r}', \omega)$  is the retarded free space Green's function. By definition,  $\psi^{\circlearrowleft}(\mathbf{r}_i) = 0$  in free space (where  $\tilde{G}_0 = G_0$ ), because the effect of the radiation-reaction in that case is already encapsulated in the resonance frequency  $\omega_0$  and linewidth  $\Gamma_0$  of the polarizability  $\alpha(\omega)$ .

By introducing the effective exciting field  $\tilde{\psi}_i = \psi_i - \psi^{\circlearrowleft}(\mathbf{r}_i)$  and local polarizability  $\tilde{\alpha}(\mathbf{r}_i, \omega) = \alpha(\omega)\psi_i/\tilde{\psi}_i$ , we can rewrite the coupled dipole equations (A1) and (A2) as Eqs. (1) and (2), where  $\tilde{\alpha}(\mathbf{r}_i, \omega)$  is given in Eq. (4). Similar renormalization procedures for the polarizability due to the environment can be found in the literature; see, for example, Refs. [64,65].

#### APPENDIX B: NUMERICAL COMPUTATION OF $\Delta G_0(\mathbf{r}_i, \omega)$

In order to explicitly calculate the renormalization contribution  $\Delta G_0(\mathbf{r}_i,\omega)$  appearing in Eq. (4), two strategies can be adopted. Using the Poisson summation formula, we can write it as

$$\Delta G_0(\mathbf{r}_i, \omega) = \sum_{n \in \mathbb{Z}^*} (-1)^n G_0(\mathbf{r}_i, \mathbf{r}_i^{(n)}, \omega),$$
 (B1)

where  $\mathbf{r}_i^{(n)}$  are the positions of the mirror images of the resonator located in  $\mathbf{r}_i$ :  $\mathbf{r}_i^{(n)} = (x_i, nW + y_i)$  if |n| is even, and  $\mathbf{r}_i^{(n)} = (x_i, (n+1)W - y_i)$  if |n| is odd. However, in practice, this sum is slowly converging. Alternatively, we may use a modal expansion of the Green's function  $\tilde{G}_0$ , such as the one given in Eq. (3), but we need to properly account for the fact that both  $\tilde{G}_0(\mathbf{r}_i, \mathbf{r}_i, \omega)$  and  $G_0(\mathbf{r}_i, \mathbf{r}_i, \omega)$  diverge, although their difference does not. This can be done by replacing  $G_0(\Delta x, \Delta y) \equiv G_0(\mathbf{r}, \mathbf{r}')$  (with  $\Delta x = x - x'$ ,  $\Delta y = y - y'$ ) by its convolution with a Gaussian function of finite

width *b* along the *y* direction,  $G_0^{(b)}(\Delta x, \Delta y) = G_0(\Delta x, \Delta y) \otimes e^{-\Delta y^2/2b^2}/\sqrt{2\pi}b$ , and using the relation

$$\Delta G_0(\mathbf{r}_i, \omega) = e^{\frac{k^2 b^2}{2}} \sum_{n \in \mathbb{Z}} (-1)^n G_0^{(b)} \left( \mathbf{r}_i, \mathbf{r}_i^{(n)}, \omega \right) - G_0^{(b)}(\mathbf{r}_i, \mathbf{r}_i, \omega),$$
(B2)

which holds for  $kb \ll 1$ . Explicit calculation gives

$$\Delta G_0(\mathbf{r}_i, \omega) = \sum_{n>0} \frac{e^{(k^2 - \pi^2 n^2 / W^2)b^2 / 2}}{4ik_n W} (1 - e^{2i\pi n y_i / W})$$
$$- \frac{\gamma + \ln(b^2 k^2 / 8) - i\pi}{4\pi} + \mathcal{O}(kb), \quad (B3)$$

where  $\gamma$  is the Euler-Mascheroni constant. Simulation results presented in this article have been obtained by computing the polarizability  $\tilde{\alpha}(\mathbf{r}_i, \omega)$  defined in Eq. (4) with expression (B3) for each scatterer position  $\mathbf{r}_i$ . Convergence is reached for a number of terms in Eq. (B3) of the order of  $\mu N_s$ , with  $\mu \gg 1$ .

- Z. Shi and A. Z. Genack, Transmission eigenvalues and the bare conductance in the crossover to Anderson localization, Phys. Rev. Lett. 108, 043901 (2012).
- [2] R. Sarma, A. G. Yamilov, S. Petrenko, Y. Bromberg, and H. Cao, Control of energy density inside a disordered medium by coupling to open or closed channels, Phys. Rev. Lett. 117, 086803 (2016).
- [3] N. Bender, A. Yamilov, A. Goetschy, H. Yılmaz, C. W. Hsu, and H. Cao, Depth-targeted energy delivery deep inside scattering media, Nat. Phys. 18, 309 (2022).
- [4] S. M. Popoff, G. Lerosey, R. Carminati, M. Fink, A. C. Boccara, and S. Gigan, Measuring the transmission matrix in optics: An approach to the study and control of light propagation in disordered media, Phys. Rev. Lett. 104, 100601 (2010).
- [5] C. W. Hsu, S. F. Liew, A. Goetschy, H. Cao, and A. D. Stone, Correlation-enhanced control of wave focusing in disordered media, Nat. Phys. 13, 497 (2017).
- [6] Y. Choi, C. Yoon, M. Kim, T. D. Yang, C. Fang-Yen, R. R. Dasari, K. J. Lee, and W. Choi, Scanner-free and wide-field endoscopic imaging by using a single multimode optical fiber, Phys. Rev. Lett. 109, 203901 (2012).
- [7] M. Plöschner, T. Tyc, and T. Čižmár, Seeing through chaos in multimode fibres, Nat. Photon. 9, 529 (2015).
- [8] M. W. Matthès, Y. Bromberg, J. de Rosny, and S. M. Popoff, Learning and avoiding disorder in multimode fibers, Phys. Rev. X 11, 021060 (2021).
- [9] A. Badon, V. Barolle, K. Irsch, A. C. Boccara, M. Fink, and A. Aubry, Distortion matrix concept for deep optical imaging in scattering media, Sci. Adv. 6, eaay7170 (2020).
- [10] H. Lee, S. Yoon, P. Loohuis, J. H. Hong, S. Kang, and W. Choi, High-throughput volumetric adaptive optical imaging using compressed time-reversal matrix, Light Sci. Appl. 11, 16 (2022).
- [11] A. Lagendijk, A. P. Mosk, M. Fink, and G. Lerosey, Controlling waves in space and time for imaging and focusing in complex media (review), Nat. Photon. 6, 283 (2012).

- [12] H. Cao, A. P. Mosk, and S. Rotter, Shaping the propagation of light in complex media, Nat. Phys. **18**, 994 (2022).
- [13] C. Texier, Wigner time delay and related concepts: Application to transport in coherent conductors, Physica E 82, 16 (2016).
- [14] S. Rotter and S. Gigan, Light fields in complex media: Mesoscopic scattering meets wave control, Rev. Mod. Phys. 89, 015005 (2017).
- [15] M. Durand, S. M. Popoff, R. Carminati, and A. Goetschy, Optimizing light storage in scattering media with the dwell-time operator, Phys. Rev. Lett. 123, 243901 (2019).
- [16] A. Yariv, Y. Xu, R. K. Lee, and A. Scherer, Coupled-resonator optical waveguide: A proposal and analysis, Opt. Lett. 24, 711 (1999).
- [17] A. Goetschy and S. E. Skipetrov, Euclidean matrix theory of random lasing in a cloud of cold atoms, Europhys. Lett. 96, 34005 (2011).
- [18] C. W. Hsu, B. Zhen, A. D. Stone, J. D. Joannopoulos, and M. Soljacic, Bound states in the continuum, Nat. Rev. Mater. 1, 16048 (2016).
- [19] M. F. Limonov, M. V. Rybin, A. N. Poddubny, and Y. S. Kivshar, Fano resonances in photonics, Nat. Photon. 11, 543 (2017).
- [20] E. Shahmoon, D. S. Wild, M. D. Lukin, and S. F. Yelin, Cooperative resonances in light scattering from two-dimensional atomic arrays, Phys. Rev. Lett. 118, 113601 (2017).
- [21] P. Lalanne, W. Yan, K. Vynck, C. Sauvan, and J.-P. Hugonin, Light interaction with photonic and plasmonic resonances, Laser Photon. Rev. 12, 1700113 (2018).
- [22] D. E. Chang, J. S. Douglas, A. González-Tudela, C.-L. Hung, and H. J. Kimble, *Colloquium*: Quantum matter built from nanoscopic lattices of atoms and photons, Rev. Mod. Phys. 90, 031002 (2018).
- [23] P. del Hougne, R. Sobry, O. Legrand, F. Mortessagne, U. Kuhl, and M. Davy, Experimental realization of optimal energy storage in resonators embedded in scattering media, Laser Photon. Rev. 15, 2000335 (2021).

- [24] P. Hong, O. S. Ojambati, A. Lagendijk, A. P. Mosk, and W. L. Vos, Three-dimensional spatially resolved optical energy density enhanced by wavefront shaping, Optica 5, 844 (2018).
- [25] G. Labeyrie, E. Vaujour, C. A. Müller, D. Delande, C. Miniatura, D. Wilkowski, and R. Kaiser, Slow diffusion of light in a cold atomic cloud, Phys. Rev. Lett. 91, 223904 (2003).
- [26] R. Sapienza, P. D. García, J. Bertolotti, M. D. Martín, A. Blanco, L. Viña, C. López, and D. S. Wiersma, Observation of resonant behavior in the energy velocity of diffused light, Phys. Rev. Lett. 99, 233902 (2007).
- [27] B. Tallon, T. Brunet, and J. H. Page, Impact of strong scattering resonances on ballistic and diffusive wave transport, Phys. Rev. Lett. 119, 164301 (2017).
- [28] F. Lemoult, N. Kaina, M. Fink, and G. Lerosey, Wave propagation control at the deep subwavelength scale in metamaterials, Nat. Phys. 9, 55 (2013).
- [29] L. V. Hau, S. E. Harris, Z. Dutton, and C. H. Behroozi, Light speed reduction to 17 metres per second in an ultracold atomic gas, Nature (London) **397**, 594 (1999).
- [30] A. Lagendijk and B. A. van Tiggelen, Resonant multiple scattering of light, Phys. Rep. 270, 143 (1996).
- [31] R. Pierrat, B. Grémaud, and D. Delande, Enhancement of radiation trapping for quasiresonant scatterers at low temperature, Phys. Rev. A **80**, 013831 (2009).
- [32] P. Weiss, M. O. Araújo, R. Kaiser, and W. Guerin, Subradiance and radiation trapping in cold atoms, New J. Phys. 20, 063024 (2018).
- [33] A. Glicenstein, A. Apoorva, D. B. Orenes, H. Letellier, A. M. G. de Melo, R. Saint-Jalm, and R. Kaiser, *In situ* measurements of light diffusion in an optically dense atomic ensemble, Phys. Rev. Lett. 133, 233401 (2024).
- [34] E. Akkermans and G. Montambaux, *Mesoscopic Physics of Electrons and Photons* (Cambridge University Press, Cambridge, 2007).
- [35] D. S. Fisher and P. A. Lee, Relation between conductivity and transmission matrix, Phys. Rev. B 23, 6851 (1981).
- [36] C. W. J. Beenakker, Random-matrix theory of quantum transport, Rev. Mod. Phys. **69**, 731 (1997).
- [37] R. Carminati and J. Schotland, *Principles of Scattering and Transport of Light* (Cambridge University Press, Cambridge, 2021).
- [38] R. Monsarrat, R. Pierrat, A. Tourin, and A. Goetschy, Pseudogap and Anderson localization of light in correlated disordered media, Phys. Rev. Res. 4, 033246 (2022).
- [39] O. Dorokhov, On the coexistence of localized and extended electronic states in the metallic phase, Solid State Commun. **51**, 381 (1984).
- [40] P. A. Mello, P. Pereyra, and N. Kumar, Macroscopic approach to multichannel disordered conductors, Ann. Phys. (NY) 181, 290 (1988).
- [41] Y. Imry, Active transmission channels and universal conductance fluctuations, Europhys. Lett. 1, 249 (1986).
- [42] V. A. Gopar and R. A. Molina, Controlling conductance statistics of quantum wires by driving ac fields, Phys. Rev. B **81**, 195415 (2010).
- [43] A. Abrikosov, The paradox with the static conductivity of a onedimensional metal, Solid State Commun. 37, 997 (1981).
- [44] M. Davy, Z. Shi, J. Park, C. Tian, and A. Genack, Universal structure of transmission eigenchannels inside opaque media, Nat. Commun. 6, 6893 (2015).

- [45] P. Fang, C. Tian, L. Zhao, Y. P. Bliokh, V. Freilikher, and F. Nori, Universality of eigenchannel structures in dimensional crossover, Phys. Rev. B 99, 094202 (2019).
- [46] A. Ishimaru, Wave Propagation and Scattering in Random Media (Oxford University Press, Tokyo, 1997).
- [47] A. Peña, A. Girschik, F. Libisch, S. Rotter, and A. A. Chabanov, The single-channel regime of transport through random media, Nat. Commun. 5, 3488 (2014).
- [48] M. Davy and A. Z. Genack, Selectively exciting quasi-normal modes in open disordered systems, Nat. Commun. 9, 4714 (2018).
- [49] L. Landau, L. Pitaevskii, and E. Lifshitz, *Electrodynamics of Continuous Media*, 2nd ed. (Elsevier, Moscow, 1984), Vol. 8.
- [50] E. P. Wigner, Lower limit for the energy derivative of the scattering phase shift, Phys. Rev. 98, 145 (1955).
- [51] F. T. Smith, Lifetime matrix in collision theory, Phys. Rev. 118, 349 (1960).
- [52] R. Pierrat, P. Ambichl, S. Gigan, A. Haber, R. Carminati, and S. Rotter, Invariance property of wave scattering through disordered media, Proc. Natl. Acad. Sci. USA 111, 17765 (2014).
- [53] C. Texier and A. Comtet, Universality of the Wigner time delay distribution for one-dimensional random potentials, Phys. Rev. Lett. 82, 4220 (1999).
- [54] A. Ossipov, T. Kottos, and T. Geisel, Statistical properties of phases and delay times of the one-dimensional Anderson model with one open channel, Phys. Rev. B 61, 11411 (2000).
- [55] C. J. Bolton-Heaton, C. J. Lambert, V. I. Fal'ko, V. Prigodin, and A. J. Epstein, Distribution of time constants for tunneling through a one-dimensional disordered chain, Phys. Rev. B 60, 10569 (1999).
- [56] A. Ossipov, Scattering approach to Anderson localization, Phys. Rev. Lett. 121, 076601 (2018).
- [57] T. Kottos, Statistics of resonances and delay times in random media: Beyond random matrix theory, J. Phys. A: Math. Gen. 38, 10761 (2005).
- [58] D. Laurent, O. Legrand, P. Sebbah, C. Vanneste, and F. Mortessagne, Localized modes in a finite-size open disordered microwave cavity, Phys. Rev. Lett. 99, 253902 (2007).
- [59] G. J. Aubry, L. S. Froufe-Pérez, U. Kuhl, O. Legrand, F. Scheffold, and F. Mortessagne, Experimental tuning of transport regimes in hyperuniform disordered photonic materials, Phys. Rev. Lett. 125, 127402 (2020).
- [60] L. A. Razo-López, G. J. Aubry, F. A. Pinheiro, and F. Mortessagne, Strong localization of microwaves beyond two dimensions in aperiodic Vogel spirals, Phys. Rev. B 109, 014205 (2024).
- [61] A. G. Yamilov, R. Sarma, B. Redding, B. Payne, H. Noh, and H. Cao, Position-dependent diffusion of light in disordered waveguides, Phys. Rev. Lett. 112, 023904 (2014).
- [62] M. Lee, H. Hong, J. Yu, F. Mujid, A. Ye, C. Liang, and J. Park, Wafer-scale  $\delta$  waveguides for integrated two-dimensional photonics, Science **381**, 648 (2023).
- [63] H. Ling, J. B. Khurgin, and A. R. Davoyan, Atomic-void van der Waals channel waveguides, Nano Lett. 22, 6254 (2022).
- [64] L. Novotny and B. Hecht, *Principles of Nano-Optics* (Cambridge University Press, Cambridge, 2012).
- [65] E. Castanié, R. Vincent, R. Pierrat, and R. Carminati, Absorption by an optical dipole antenna in a structured environment, Int. J. Opt. 2012, 452047 (2012).